Analyst

Check for updates

In situ synthesis of gold-core silver-shell nanoparticles on bacterial cellulose for SERS detection of micro- and nanoplastic particles in vegetables

Seyedehalaleh Koushah, Azlin Mustapha and Mengshi Lin [iD] *

Micro- and nanoplastic particles (MNPs) are ubiquitous environmental contaminants, raising significant concerns due to their potential health risks. There is an urgent need for highly sensitive detection methods, especially for complex food samples. This study presents a novel surface-enhanced Raman spectroscopy (SERS) sensor, developed through *in situ* synthesis of gold-core silver-shell (Au@Ag) nanoparticles on bacterial cellulose (BC), for detecting MNPs in leafy vegetables. The BC serves as both a biocompatible scaffold and an eco-friendly reducing agent, thereby facilitating the green synthesis of nanoparticles. The BC@Au@Ag sensor enabled reliable detection of polyethylene (PE) and polystyrene (PS) micro- and nanoplastics in kale samples at 4 mg kg^{-1}, while the theoretically estimated limits of detection, calculated from weighted regression analysis, were as low as 1.22 mg kg^{-1} for PS and 3.95 mg kg^{-1} for PE. Combined recovery and precision analyses confirm the reproducibility and robustness of the BC@Au@Ag SERS platform, demonstrating its suitability for sensitive and reliable monitoring of MNPs in complex food matrices.

Introduction

Plastics, valued for their affordability, durability, and versatility, are integral to modern life. However, their widespread use has caused significant environmental contamination, particularly through degradation into micro- and nanoplastics (MNPs), which pose substantial risks to ecosystems and human health.[1] U.S. plastic production reached approximately 130 billion pounds in 2023, reflecting continued growth in the sector.[2] Microplastics are defined as plastic fragments measuring between 5 mm and 100 nm, while nanoplastics are those smaller than 100 nm.[3] The persistence and mismanagement of plastic waste have resulted in the widespread presence of MNPs in air, soil, water, and even remote locations. Alarmingly, MNPs have been detected in the human body, including blood, placenta, and breast milk, raising concerns about their toxicological effects. Their infiltration into the food chain is particularly concerning, with MNPs found in agricultural crops, seafood, processed foods, and beverages. Given the escalating prevalence of plastic pollution, developing reliable, cost-effective methods for detecting and quantifying MNPs is critical for mitigating their health and environmental risks.[4,5]

Food Science Program, Division of Food, Nutrition & Exercise Sciences, University of Missouri, Columbia, MO, 65211, USA. E-mail: linme@missouri.edu

Detecting MNPs in food samples is challenging due to their diverse compositions, varying particle sizes, and interactions with co-contaminants.[5] Conventional analytical techniques, such as Fourier-transform infrared spectroscopy (FTIR),[6,7] pyrolysis gas chromatography-mass spectrometry (Pyr-GC-MS),[8] and field flow fractionation,[9] have been employed for MNP characterization. However, these methods are limited by high cost, labor-intensive sample preparation, and poor sensitivity at the nanoscale. For instance, while Pyr-GC-MS provides precise chemical composition analysis, its expense and time-consuming nature make it impractical for large-scale monitoring.[10] These limitations have fuelled interest in surface-enhanced Raman spectroscopy (SERS), which combines high sensitivity, molecular specificity, and rapid analysis with minimal sample preparation.[11] SERS leverages plasmonic nanostructures to amplify weak Raman signals, enabling trace-level detection of MNPs. Additional advantages, such as non-destructive analysis, reduced contamination risk, and lower equipment and expertise requirements, position SERS as a scalable and cost-effective alternative to traditional methods.[12] Nevertheless, challenges remain, particularly in detecting low-Raman-active plastics like polyethylene (PE), which demand optimized sensor designs to enhance signal strength.[13]

The performance of SERS sensors is critically influenced by the choice of substrate. Colloidal nanoparticle suspensions offer strong enhancement but suffer from reproducibility

issues due to aggregation.[14] Solid substrates, such as glass or silicon wafers, improve stability but are costly and complex to fabricate.[15,16] Recently, Liu *et al.* (2024) introduced a two-phase (ethyl acetate–water) SERS platform in which silver nanoparticles self-assembled with poly(methyl methacrylate) (PMMA) films to detect polystyrene (PS) and polyethylene terephthalate (PET) nanoplastics at trace concentrations. In this approach, Ag nanoparticles accumulated at the liquid–liquid interface and were stabilized by PMMA to form an active SERS film.[17] While the method offered exceptional sensitivity, the multi-step interfacial assembly and solvent-based preparation still pose challenges for practical or large-scale application. Fiber-based SERS sensors provide the additional advantage of remote and *in situ* detection.[18] Within this class, cellulose-based substrates are particularly attractive owing to their biocompatibility, tunable porosity, eco-friendliness, and low cost.[16] Notably, nanoparticle deposition on cellulose fiber prevents aggregation, ensuring stable SERS activity without additional stabilizers.[19] However, plant-derived cellulose suffers from heterogeneous pore size and composition, leading to variable signal intensities. To overcome this, we employed bacterial cellulose (BC), which combines high purity with a uniform pore structure, offering a robust substrate for reproducible and sensitive SERS detection.[16,20]

This study developed a green and scalable approach by synthesizing gold-core silver-shell (Au@Ag) nanoparticles *in situ* within BC, using BC itself as both a structural scaffold and reducing agent. The porous network of BC facilitates homogeneous deposition and stabilization of Au@Ag nanoparticles, enhancing their plasmonic properties for MNP detection. The resulting BC-based SERS sensor provides a highly sensitive platform for detecting PE and PS particles in food matrices, using leafy vegetables as model samples due to their susceptibility to surface contamination. By optimizing BC-based SERS sensors for agricultural products, this work advances sustainable monitoring strategies for plastic pollution in the food chain and contributes to food safety and quality assurance.

Experimental

Materials

HAuCl$_4$, AgNO$_3$, ascorbic acid, BG 11 broth, citric acid, and PS particles in two sizes (1 µm, PS1; 100 nm, PS100) were obtained from Sigma-Aldrich (St. Louis, USA). PE solutions, also in two sizes (1 µm, PE1; 65 nm, PE65), were purchased from Lab 261 (Palo Alto, CA, USA). Trisodium citrate was acquired from Alfa Aesar (Ward Hill, MA, USA), and Whatman #6 (90 mm) filter paper was supplied by Schleicher & Schuell (Maidstone, UK). NaH$_2$PO$_4$·H$_2$O and dextrose were sourced from Fisher Scientific (Fair Lawn, NJ, USA). Molasses was obtained from Good Food, Inc. (Honey Brook, PA, USA), and corn steep liquor (CSL) was purchased from Nutrabaits (Nottingham, UK). YM broth and peptone were supplied from Becton Dickson (Sparks, MD, USA). Ammonium sulfate was

sourced by Mallinckrodt Chemical Works (St. Louis, MO, USA), and 190-proof ethanol was purchased from Decon Laboratories, Inc. (King of Prussia, PA, USA). Algae were obtained from Carolina Biological Supply (Burlington, NC, USA), and organic, pre-washed leafy vegetables (spinach and kale) were purchased from a local market. *Gloconoacetobacter hansenii* (*G. hansenii*) was also used.

Bacterial cellulose fabrication

The BC membrane was fabricated under static conditions using a modified Hestrin-Schramm (mHS) culture medium, consisting of NaH$_2$PO$_4$·H$_2$O (0.27% w/v), citric acid (0.115% w/v), CSL (1.91% w/v), molasses (5.38% w/v), ammonium sulfate (0.63% w/v), and ethanol (1.38% v/v).[20] The *G. hansenii* inoculum was first pre-cultivated in the HS medium containing glucose (2.0% w/v), peptone (0.5% w/v), yeast extract (0.5% w/v), NaH$_2$PO$_4$·H$_2$O (0.27% w/v), and citric acid (0.115% w/v).[21] The pre-cultivated inoculum was then transferred to the mHS medium and incubated under static conditions for three days. After incubation, the BNC membrane was harvested, thoroughly washed with water, decolorized with a 0.1% (w/v) NaOH solution, and rinsed again with water. The purified membrane was stored at 4 °C until further use.

In situ synthesis of SERS sensor

To develop a SERS sensor incorporating core–shell nanoparticles (BC@Au@Ag), three experimental methods (M1, M2, and M3) were evaluated to determine the optimal synthesis approach, with BC serving as both the substrate and the primary reducing agent. A fourth method (M4) was included as a control. In all four methods, gold nanoparticles (AuNP) and silver nanoparticles (AgNP) were pre-synthesized prior to deposition. The gold seed solution was prepared based on a modified method from our previous study.[3,11] Specifically, HAuCl$_4$ (2.5×10^{-4} M) was reduced using a 1% (w/w) aqueous trisodium citrate solution under continuous stirring at 220 rpm while heating to the boiling point. To synthesize the AgNP solution, 90 mg of AgNO$_3$ was dissolved in 500 mL of deionized water and the solution brought to a boil. Subsequently, 10 mL of a 1% (w/w) trisodium citrate solution was added, and the mixture was boiled for 1 h.[22]

Method M1. BC sheets were immersed in the AuNP solution and incubated overnight to allow nanoparticle adsorption. After incubation, the AuNP solution was removed, and the BC sheets were washed three times with deionized water. The BC was then transferred to an AgNP solution and incubated at room temperature for 7 days with gentle agitation to ensure uniform silver deposition. The resulting BC@Au@Ag composites were rinsed thoroughly with deionized water and stored at 4 °C.

Method M2. BC particles were incubated in a mixture of 6 mL of AuNP and 2 mL of AgNP without an additional reducing agent. The incubation conditions mirrored those of Method M1 (room temperature, 7 days, gentle agitation). Post-incubation, the samples were washed with deionized water and stored at 4 °C.

Method M3. BC particles were co-incubated with 6 mL of AuNPs, 2 mL of AgNPs, and 250 mL of ascorbic acid at room temperature for 7 days under continuous mild agitation. Post-incubation, the samples were washed with deionized water and stored at 4 °C.

Method M4 (control). Au@Ag nanoparticles were synthesized separately according to Kousheh *et al.* (2024).[3] These pre-formed nanoparticles were then used to incubate BC particles under the same conditions as the other methods (room temperature, 7 days, mild agitation). Post-incubation, the samples were rinsed with deionized water and stored at 4 °C.

Characterization of SERS sensor

The BC@Au@Ag samples were characterized using transmission electron microscopy (TEM) coupled with energy-dispersive X-ray spectroscopy (EDS) to investigate the core–shell structure and nanoparticle coating on BC nanofibers. A spectra 300 STEM (ThermoFisher Scientific Inc.) equipped with EDS was used to examine the distribution, morphology, and elemental composition of the Au@Ag nanoparticles on the nanofibers. Samples were prepared by air-drying on a copper grid at room temperature and imaged at an accelerating voltage of 300 kV. TEM provided high-resolution visualization of the nanoparticles' size, shape, and dispersion, while EDS facilitated elemental analysis and mapping, confirming the successful formation of the core–shell structure.[23] These techniques offered valuable insights into the functionalization, morphology, and composition of the nanofibers, demonstrating their suitability for further analysis and applications in this study.

Sample preparation

Mixtures of PS and PE were prepared according to the specifications in Table 1. The stock suspensions of PS and PE were prepared at 1 mg mL^{-1} and used for all spiking experiments. Fresh, pre-washed spinach and kale were rinsed thoroughly and soaked in distilled water for 30 min to remove residual impurities. The cleaned leaves (10 g) were then treated with the PS and PE mixture, with final concentrations adjusted to match those outlined in Table 1. The final matrix concentrations were calculated based on the added mass of MNPs relative to the sample weight according to:

$$C_{veg}\,(mg\,kg^{-1}) = \frac{C_{stock}\,(mg\,mL^{-1}) \times V_{spike}\,(mL)}{m_{sample}\,(kg)}$$

where $C_{stock} = 1$ mg mL^{-1} and $m_{sample} = 0.01$ kg.

Table 1 Final concentrations of PS and PE solutions in water and food samples

MNP	Concentration (mg kg^{-1} or mg L^{-1})				
PS	4	10	25	50	100
PE	40	100	250	500	1000

PS: polystyrene nanoparticles; PE: polyethylene microparticles.

After applying the plastic mixture, the samples were heated at 40 °C in an oven until the spiked MNPs were completely dry. To extract the MNPs from the leaves, the dried samples were vortexed rigorously for 1 min in 4 mL of deionized water. To ensure efficient extraction, ultrasonication was applied for 5 min to detach MNPs from the leaf surfaces. The resulting suspensions were then filtered through Whatman #6 (90 mm) filter paper and prepared for subsequent analysis.

Detection by SERS

SERS analysis was conducted using a DXR2 Raman Spectrometer (ThermoFisher Inc., Waltham, MA, USA) equipped with a 785 nm diode laser. Samples were spiked onto a BC@Au@Ag substrate and dried in an oven at 40 °C before acquiring SERS spectra. To ensure consistency, all spectra were collected using identical acquisition settings: an incident laser power of 20 mW, an accumulation and exposure time of 3 s, and a spectral range of 600–1800 cm^{-1}. This range captured key vibrational modes, offering detailed molecular insights into the composition and structure of the analytes.

Data analysis

Spectral data were analyzed using IBM SPSS Statistics software (Version 19) with a 95% confidence level ($P < 0.05$). Results were expressed as mean values ± standard deviations to reflect data variability. Raman spectral data were collected and processed using OMNIC software (ThermoFisher Scientific Inc.), including noise reduction, baseline correction, peak smoothing, and resolution enhancement to ensure high-quality data for interpretation.

Calibration plots were constructed using samples spiked at five concentration levels (4, 10, 25, 50, and 100). For each level, three independent replicates were prepared and measured on independent BC@Au@Ag substrates. The SERS intensities from these replicates were averaged before regression analysis. Calibration plots were initially fitted using unweighted linear regression. Potential heteroscedasticity was assessed by inspection of residual plots and by comparison of unweighted and 1/x weighted regression models. Weighted regression was adopted when it resulted in a substantial change (≥10%) in slope and/or intercept or improved representation of the low-concentration region. For datasets where weighting did not meaningfully alter regression parameters (<9% difference), unweighted regression was retained. The regression model used for each calibration plot is explicitly reported. Regression parameters, including slope, intercept, R^2, and 95% confidence intervals for slope and intercept, were obtained from the selected regression model.

The limit of detection (LOD) and the limit of quantification (LOQ) were calculated according to ICH guidelines using:[11]

$$LOD = 3.3 \times (SD/slope)$$

$$LOQ = 10 \times (SD/slope)$$

where SD denotes the standard deviation of the SERS response at the lowest calibration level ($n = 3$). This approach was

selected because the intercept-based σ under weighted regression yielded unstable or non-physical detection limits. Accordingly, all reported LOD and LOQ values were recalculated using this method. These metrics indicate the method's sensitivity and minimum detectable concentration, supporting the evaluation of its accuracy and reliability for analyte quantification. Additionally, a calibration plots was constructed to illustrate the relationship between SERS intensity and MNP concentrations.

Results and discussion

BC@Au@Ag characterization

To develop a SERS sensor utilizing core–shell nanoparticles (BC@Au@Ag), three distinct synthetic protocols were systematically evaluated. TEM-EDS analysis was employed to assess the nanoparticle's morphology and elemental distribution. Fig. 1 illustrates the successful immobilization of nanoparticles onto BC fibers, while Fig. 2 provides a detailed visualization of the gold-silver core–shell architecture achieved through each synthesis method.

In Method M1, TEM analysis (Fig. 2A) revealed that this approach failed to yield the desired gold-silver core–shell structure. Instead, it yielded randomly distributed metallic nano-

particles, approximately 20 nm in diameter, consisting of a mixture of individual Au and Ag particles rather than a cohesive core–shell architecture. This outcome likely results from extensive interactions between the cellulose and AuNP overnight, enabling strong adsorption through hydrogen bonding, van der Waals, and electrostatic forces between Au surfaces and BC hydroxyl groups.[24] Such extensive Au–BC interactions saturated available –OH sites, leaving only a limited number of reactive hydroxyl groups for the subsequent interaction with AgNP. As a result, when silver precursor was added, AgNP diffused into the AuNP-loaded regions and coalesced with the existing gold nanoparticles, leading to a random Au–Ag mixture instead of a uniform core–shell formation. This interpretation is further corroborated by FTIR analysis of the M1 sample (Fig. 3). Before the addition of AgNP, the spectrum showed only minor changes compared to pristine BC, with attenuation of the O–H stretching band ($\sim$3297 cm^{-1}), suggesting interactions between BC hydroxyl groups and AuNP. However, the peak at 2900 cm^{-1}, attributed to C–H stretching vibrations and partially coupled O–H modes,[25] showed a marked decrease in intensity. This reduction likely reflects both partial surface coverage of C–H regions by AuNPs and the involvement of adjacent hydroxyl groups in metal–polymer interactions. After silver addition, the spectrum exhibited marginal sharpening of peaks in the
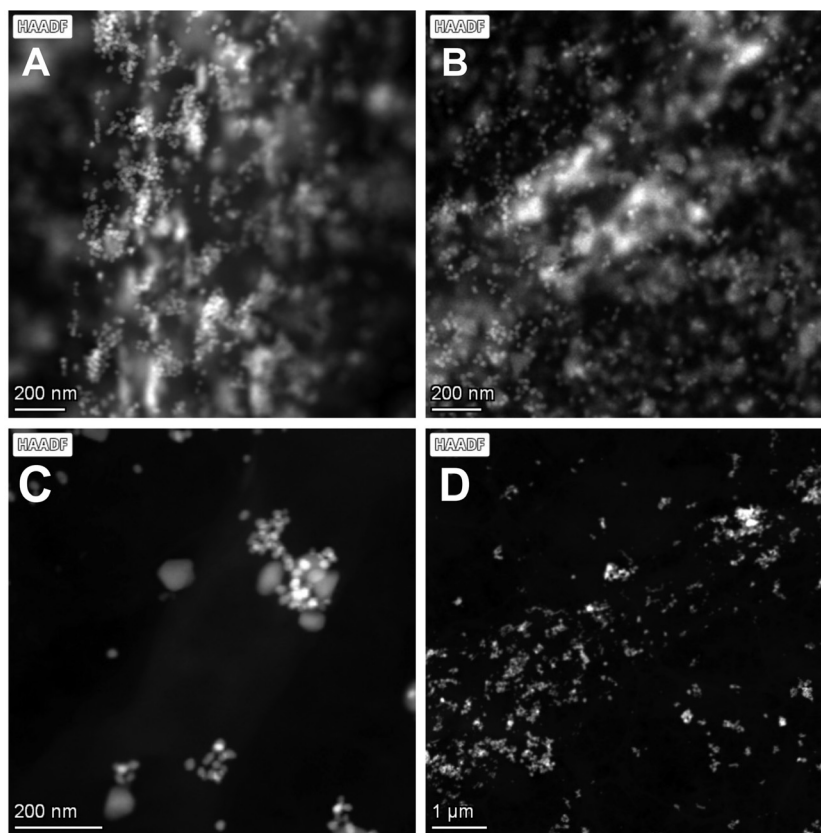

Fig. 1 TEM images showing the immobilization of Au@Ag nanoparticles on bacterial cellulose nanofibers prepared by different *in situ* synthesis methods: M1 (A), M2 (B), M3 (C), and control M4 (D).
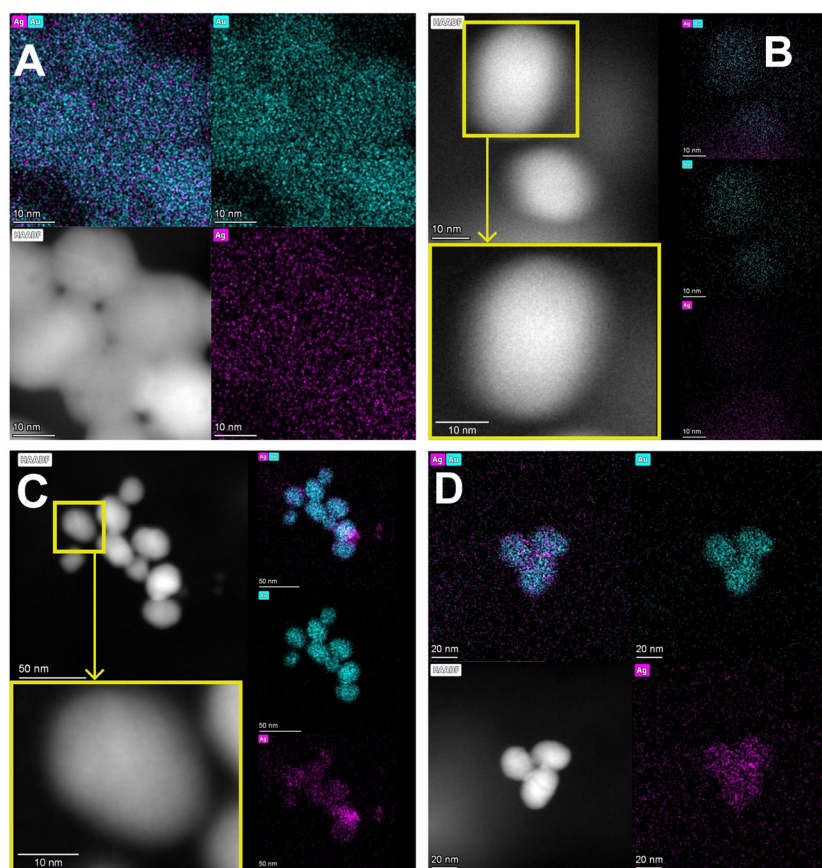
Fig. 2 TEM images of Au@Ag nanoparticles synthesized by Method M1 (A), Method M2 (B), Method M3 (C), and the control Method M4 (D), illustrating differences in core−shell morphology and completeness.
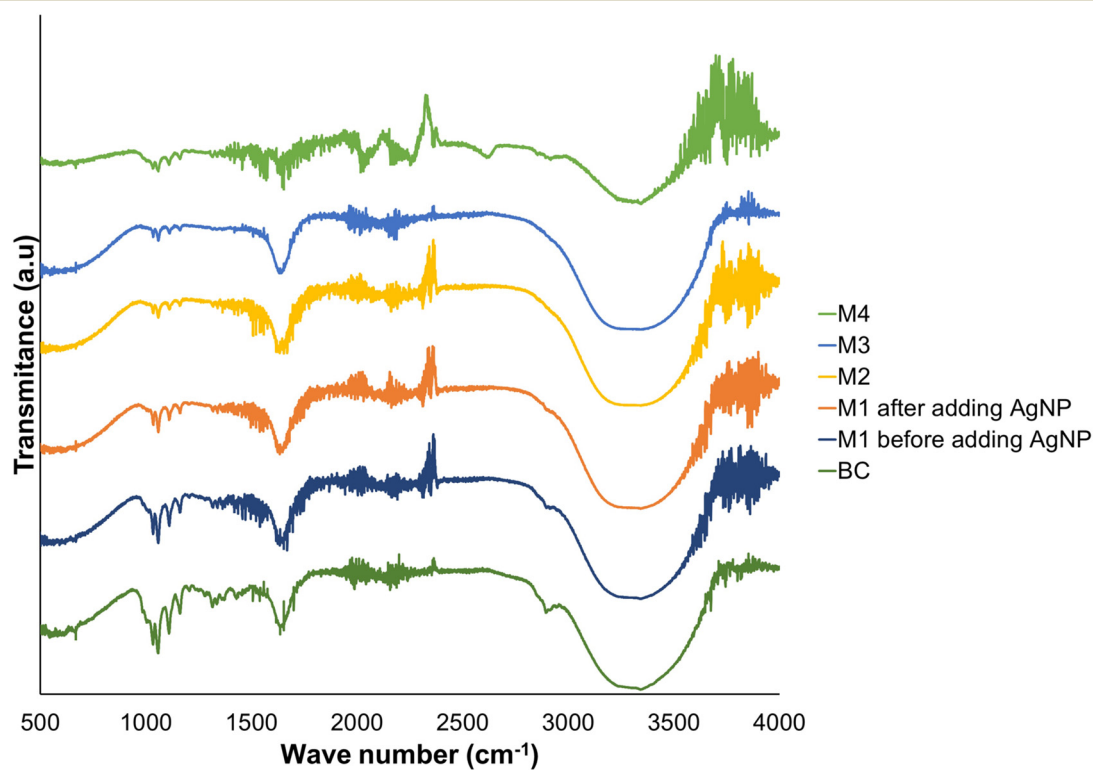

Fig. 3 FTIR spectra of bacterial cellulose (BC) and BC-based nanocomposites prepared by *in situ* synthesis methods.

$1056–1159$ cm^{-1} region, related to C–O stretching or valence vibrations of cellulose, and the 2900 cm^{-1} peak almost disappeared. These subtle spectral shifts imply limited surface interactions without significant structural integration of the nanoparticles into the cellulose matrix, consistent with findings from previous reports.[26–28]

To address the limitations of Method M1, Methods M2 and M3 were developed to expose BC directly to a mixed Au–Ag nanoparticle solution, preserving the redox functionality of the cellulose. This adjustment ensured that sufficient hydroxyl groups remained available to mediate the interaction with AgNP and facilitate shell formation. Nanoparticles produced by Methods M2 and M3 displayed well-defined core–shell architectures with uniform morphology and consistent particle sizes, as shown in Fig. 2B and C. The mean particle sizes were 25.93 ± 2.01 nm for Method M2 and 24.61 ± 1.09 nm for Method M3. Notably, particles synthesized using Method M2 exhibited only partial and ultrathin silver coverage on the core (~21 nm diameter), which is more accurately described as an Ag-rich overlayer rather than a fully developed shell. In contrast, Method M3 produced particles with a complete Ag shell of ~0.8 nm thickness on a smaller core (~15 nm diameter). These structural findings align with the FTIR spectrum of Method M2, which displayed moderate changes compared to pristine BC. The O–H stretching band near 3297 cm^{-1} showed partial attenuation, indicating some hydroxyl group involvement in nanoparticle interactions. Additionally, the fingerprint region (1033–1159 cm^{-1}) shows a significant decrease in intensity, suggesting partial nanoparticle integration into the cellulose matrix. This supports the TEM evidence of a weak or discontinuous Ag shell in Method M2, as corroborated by previous studies.[26,29]

To enhance the reducing capacity of BC and promote the formation of a thicker silver shell, Method M3 incorporated a small amount of ascorbic acid, equivalent to one-fourth the concentration used in the control synthesis (Method M4, Fig. 2D), compared to Method M2. Ascorbic acid, a known reducing agent, complements the electron-donating properties of cellulose,[30] accelerating the interaction with AgNP and improving shell formation. The resulting nanoparticles (Fig. 2C) demonstrated a clear and consistent core–shell structure, comparable in quality to those synthesized using conventional reducing agents (Fig. 2D), thus validating the effectiveness of Method M3. The precisely engineered Au@Ag core–shell nanoparticles from Method M3 displayed optimal surface plasmon resonance characteristics, essential for maximizing SERS signal enhancement. This structural uniformity ensures high sensitivity for
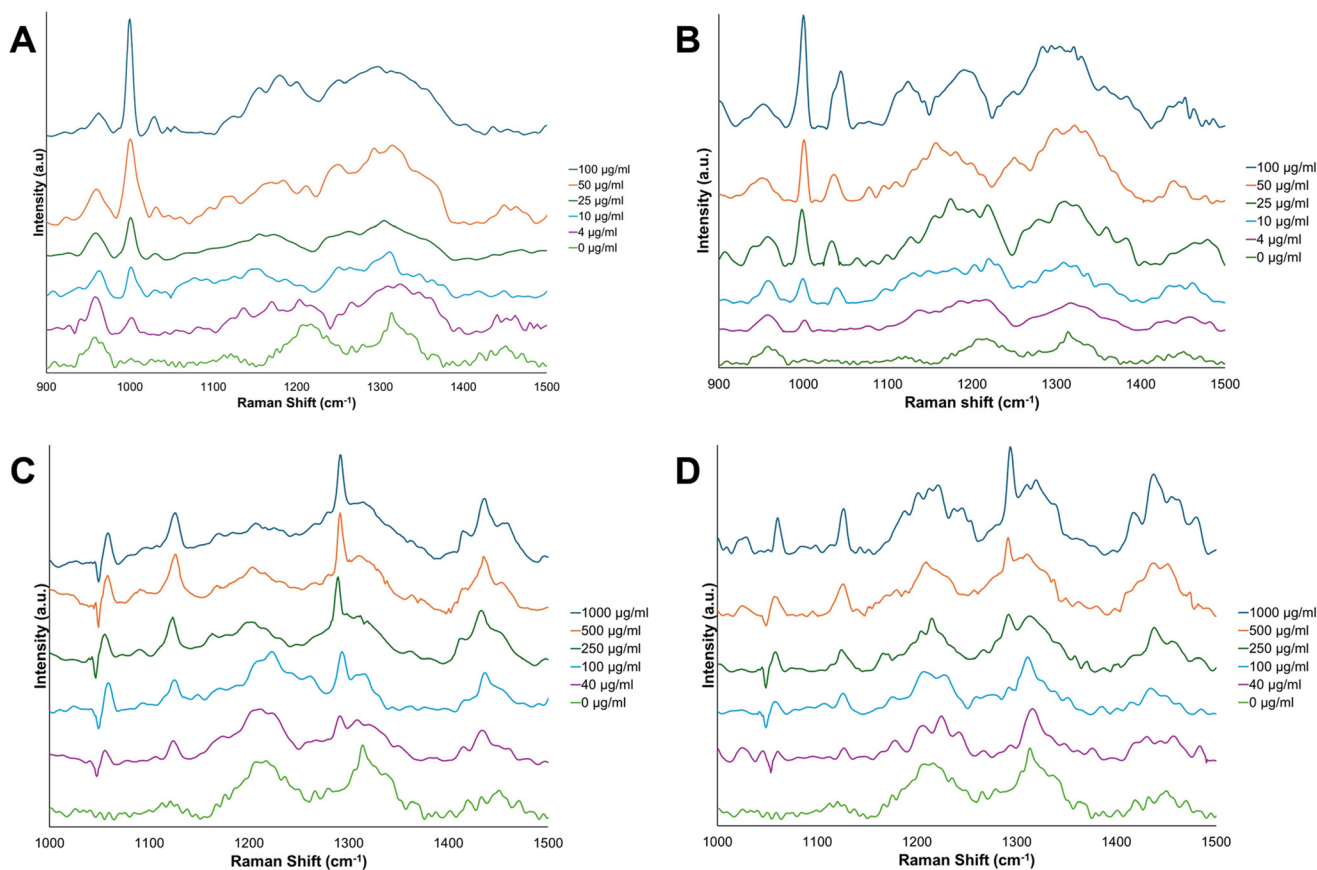

Fig. 4 SERS spectra of 1 µm polystyrene (A), 100 nm polystyrene (B), 1 µm polyethylene (C), and 65 nm polyethylene (D) MNPs in water, obtained using the BC@Au@Ag SERS sensor. The spectrum labeled "0 µg/ml" corresponds to the control (BC@Au@Ag sensor in pure water, no plastics added).

detecting trace levels of analytes, confirming the suitability of the nanocomposite for advanced sensing applications.

FTIR spectroscopy provided evidence of enhanced chemical interactions in the M3 sample. Notably, the C–H stretching band near 2900 cm^{-1}, typically associated with aliphatic –CH and –CH$_2$ vibrations in the cellulose backbone, was no longer detectable. This absence suggests significant masking of aliphatic C–H environments, likely due to strong surface coordination between cellulose chains and the densely deposited Au@Ag nanoparticles. Such interactions may restrict vibrational freedom or cause the C–H signals to overlap with broadened metal–ligand absorption bands, effectively suppressing the C–H peak.[26,31] Additionally, sharp and intensified bands in the 1033–1159 cm^{-1} region, corresponding to C–O–C glycosidic linkages and secondary alcohol C–O stretching vibrations, confirmed deeper structural integration of the metal nanoparticles into the BC matrix, consistent with the formation of a robust metal–polymer interface.

As a control, Method M4 employed pre-synthesized Au@Ag core–shell nanoparticles incubated with BC under conditions identical to those of the other methods. This *ex situ* approach was designed to evaluate whether preformed nanoparticles could integrate into the BC matrix without *in situ* reduction. The FTIR spectrum of the M4 sample revealed partial attenuation of characteristic BC signals, particularly in the fingerprint region (1033–1159 cm^{-1}), associated with C–O–C glycosidic linkages and C–O stretching, as well as a reduced O–H stretching band near 3297 cm^{-1}. These changes suggest minimal chemical interaction between the BC and the pre-synthesized Au@Ag nanoparticles. A weak band at ~2626 cm^{-1} was observed, which likely originates from residual organic stabilizers associated with the pre-synthesized Au@Ag nanoparticles. The use of trisodium citrate and ascorbic acid during synthesis can leave carboxylate- and hydroxyl-containing residues on nanoparticle surfaces, producing C–H stretching vibrations. The absence of this band in pure BC confirms its association with nanoparticle-bound organic species rather than cellulose.[32] Additionally, a peak at 2340 cm^{-1}, corresponding to CO$_2$ asymmetric stretching, was detected, likely an environmental artifact from atmospheric CO$_2$ adsorption during spectral acquisition, which is common in porous, hydrophilic matrices such as BC.[33] Notably, the H–O–H bending vibration at ~1635 cm^{-1}, typically indicative of adsorbed water, was largely absent in the M4 sample. This absence may be attributed to surface masking by nanoparticles, which could limit water retention in the IR-probed region or suppress the band due to localized surface plasmon effects disrupting hydrogen bonding between water and cellulose.[26]

Taken together, these findings suggest that the nanoparticles in the M4 sample exhibit only weak surface-level interactions with BC. The attenuated cellulose signals likely result from physical coverage of the BC surface by the metallic nanoparticles, which inhibits IR absorption from the underlying polymer rather than indicating strong chemical bonding. Consequently, the spectra reflect both signal suppression due to optical shielding by the nanoparticles and dominant spectral features of the metallic phase, consistent with incomplete integration into the cellulose matrix.

SERS measurement and characterization of MNPs

The BC@Au@Ag substrate enabled sensitive SERS detection of both PS and PE MNPs. These polymers were selected due to their ubiquity in food chains, potential implications for human health and persistence in the environment. For PS, a prominent Raman peak at 1000 cm^{-1}, corresponding to the C–C ring breathing mode, was observed (Fig. 4A and B). At higher PS concentrations, an additional peak at 1031 cm^{-1} emerged due to the deformation of C–H.[34] A slight blue shift of PS peaks was noted relative to reference spectra, likely arising from physicochemical interactions with the BC scaffold. Hydrogen bonding or changes in the local dielectric constant within the BC matrix may perturb vibrational modes, subtly altering their frequencies. For PE (Fig. 4C and D), characteristic peaks included the methine (CH) twisting vibration at 1292 cm^{-1}, C–C stretching at 1059 and 1127 cm^{-1}, and CH$_2$ bending between 1415–1460 cm^{-1}.[3,35] A small red shift was observed, which may reflect differences in polymer–substrate interactions compared to PS.

The enhanced SERS performance of the BC@Au@Ag substrate arises from the combined effects of the Au@Ag core–shell nanostructure and the BC scaffold. The silver shell generates abundant hot spots while the gold core provides stability, enabling robust plasmonic enhancement.[36,37] Plastics interact with the core–shell surface through multiple mechanisms, including π–π interactions between PS aromatic rings and the metal surface,[38] and van der Waals forces for PE, which lacks aromaticity.[13,39] The BC nanofibrillar network further amplifies these effects by immobilizing nanoparticles, preventing aggregation, and facilitating efficient retention of hydrophobic polymers within hydrophilic–hydrophobic interfaces. This synergistic configuration ensures stronger and more uniform electromagnetic fields, improved adsorption, and greater substrate stability, collectively enabling reproducible detection of PS and PE in both aqueous and complex food matrices.[3,13]

Background contributions from the BC substrate were also evident. A broader band between 1200–1400 cm^{-1}, corresponds to cellulose vibrational modes such as H–C–C, H–C–O, H–C–H bending.[40] The signal at 960 cm^{-1} are assigned to C–C and C–O stretching modes. Furthermore, bands between 1160 and 1203 cm^{-1} correspond to combined bending involving C–C–H, O–C–H, C–O–H, and stretching of C–C, C–O–C, and C–O.[41]

To evaluate performance in realistic food matrices, spinach and kale were selected as representative leafy vegetables. Characteristic vibrational modes of both PE and PS were clearly detected in these tissues (Fig. 5) and these spectra closely mirrored those obtained in aqueous suspensions. This concordance underscores the robustness and reliability of their Raman fingerprints across different matrices. However, slight red shifts in certain peaks were observed in the food
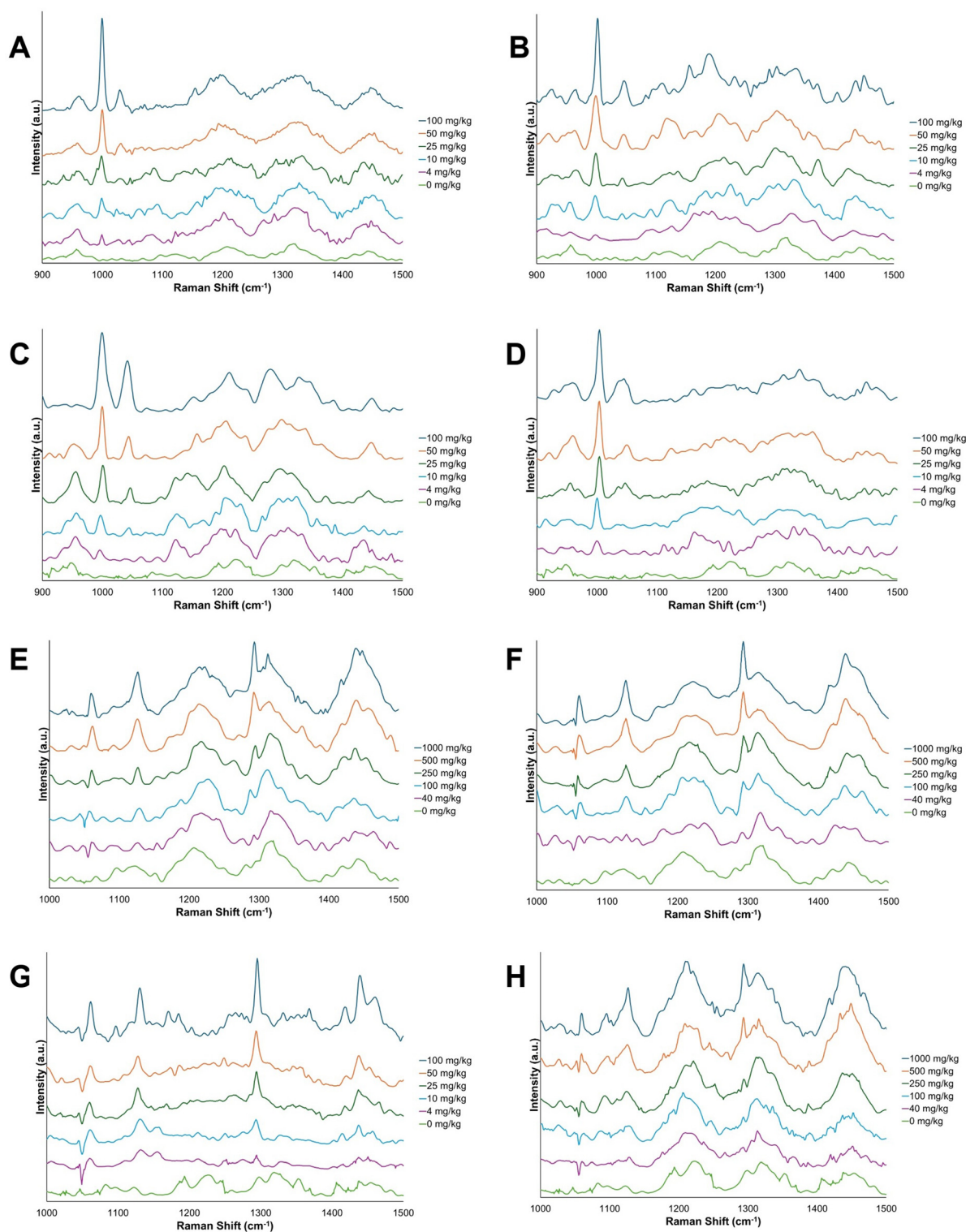
Fig. 5 SERS spectra of 1 μm polystyrene (A and C), 100 nm polystyrene (B and D), 1 μm polyethylene (E and G), and 65 nm polyethylene (F and H) MNPs in different concentrations in kale (A, B, E, and F) and spinach (C, D, G, and H) samples using the BC@Au@Ag SERS sensor (the "0 mg/kg" corresponds to the control sample which is BC@Au@Ag sensor with spinach or kale matrix, no added plastics).

samples, suggesting potential physicochemical interactions between MNPs and intrinsic food constituents. These interactions may arise from non-covalent binding between the surface functionalities of MNPs and plant biomolecules, such as phenolics, polysaccharides, proteins, and lipids.[42] Such interactions could alter the local dielectric environment

around MNPs or modify the conformation of surface-bound molecules, thereby subtly affecting the Raman signals.

The lowest detected concentration (LDC) achieved in this study was 10 mg kg^{-1} for PS and 40 mg kg^{-1} for PE in both aqueous and food matrices. These thresholds represent a clear improvement over prior reports. For example, Kousheh et al. (2024) reported detection limits of 10 mg mL^{-1} in vegetables and water,[3] and Caldwell et al. (2021) achieved 6.25 μg ml^{-1} in water samples.[43] Similarly, the LDC for PE (40 μg ml^{-1} for both PE1 and PE65) marks a significant advancement compared to earlier studies, where detection thresholds commonly exceeded 100 μg ml^{-1}.[3,13] This enhanced sensitivity is attributed to the synergistic architecture of the BC@Ag@Au sensor. The nanofibrillar cellulose matrix acts as a porous, high-surface-area scaffold that immobilizes the core–shell nanoparticles in a uniform distribution, preventing aggregation and maintaining dense plasmonic junctions. Furthermore, the bimetallic configuration improves plasmonic resonance and provides superior stability compared to single-metal substrates, while the BC scaffold promotes efficient adsorption of hydrophobic plastics and stabilizes hot spots in three dimensions. Together, these effects enhance signal reproducibility and reduce detection thresholds in complex matrices. To clearly contextualize these detection thresholds relative to previously reported SERS-based MNP studies, a summary comparison table of LOD/LOQ values across matrices and literature reports has been provided (Table 2).

Calibration plots (Fig. 6) showed monotonic, concentration-dependent SERS responses for PS and PE in both water and vegetable matrices, thereby supporting the use of the BC-based SERS platform for MNP detection. Regression models (unweighted or weighted $1/x$) were selected based on variance patterns and the sensitivity of regression parameters, as detailed in Table S1. In water, the analytes exhibited stable concentration–response trends, whereas greater signal variability was observed in spinach and kale, consistent with matrix-induced scattering, surface heterogeneity, and background interference typical of complex food systems. Consequently, R^2 values varied across particle–matrix combinations, and calibration performance was assessed primarily using residual behavior, confidence intervals of regression parameters, and the stability of LOD/LOQ estimates, rather than relying solely on R^2. Particle-size effects were both polymer- and matrix-dependent. Stronger concentration-dependent response observed for PS nanoparticles (100 nm) across matrices is likely due to their higher surface-area-to-volume ratio, which increases contact with plasmonic hot spots and enhances adsorption within the porous BC network. In contrast, PE exhibited matrix-dependent size effects, reflecting differences in particle–matrix and particle–substrate interactions. In water, larger PE particles (1 μm) likely experience more stable electromagnetic coupling due to reduced aggregation and more uniform exposure to hot spots. However, in spinach and kale matrices, smaller PE nanoparticles (65 nm) may be more efficiently entrapped within the BC fibrillar network and plant-derived surface structures, leading to enhanced local field interactions and stronger SERS signals.[44]

The LOD and LOQ values for water and food samples are summarized in Table 3. This work demonstrates a substantial reduction in detection limits for both PS and PE across nano- and microscale sizes compared to previous studies. For instance, study using Au@Ag colloids have typically reported LODs between 172.78–744.29 mg kg^{-1} and LOQs of 523.57–2255.43 mg kg^{-1},[3] while Mikac et al. (2023) observed an LOQ of 200 mg kg^{-1} for PE using gold colloids.[13] Lv et al. (2020) reported even higher thresholds for microscale PE (5000 mg kg^{-1} for 10 μm), though lower values for nanoscale PS (40 mg kg^{-1} for 500 nm and 100 nm).[22] In contrast, the BC@Ag@Au scaffold developed in this study achieved consistently low estimated LODs and LOQs across matrices, with the lowest values of 1.22 mg kg^{-1} (LOD) and 3.70 mg kg^{-1} (LOQ) for PS100 in Kale. This study also demonstrated a significant reduction in the detection threshold gap between nano- and microplastics, highlighting the improved analytical performance of the developed platform. For instance, in spinach samples, the LOD and LOQ for PE1 were determined to be 62.56 mg kg^{-1} and 189.59 mg kg^{-1}, respectively, while PS1 exhibited markedly lower thresholds of 30.36 mg kg^{-1} and 36.16 mg kg^{-1}. These findings represent a considerable advancement compared to earlier reports, where large discrepancies between PS and PE detection limits were consistently observed. For example, Mikac et al. (2023) reported LODs of 200 μg mL^{-1} for PE (4 and 1 μm) compared with 6.5 μg mL^{-1} for PS (350 nm),[13] whereas Caldwell et al. (2021) detected PS at 1.25 μg mL^{-1} (33 nm) but failed to detect PE altogether.[43] Similarly, Kousheh et al. (2024) reported thresholds of 100 mg

Table 2 Comparative evaluation of the proposed BC@Au@Ag SERS method against previously published SERS techniques for PS and PE particle detection

MNP type	Size	Substrate type	Matrix	LOC	Ref.
PS	33 nm	Ag colloid	Water	~1.25 mg mL^{-1}	Caldwell et al. (2021)[43]
PS	500 nm, 100 nm	Au NPs	Water	40 mg mL^{-1}	Lv et al. (2020)[22]
PE	1–4 μm	Au colloid	Water	200 mg mL^{-1}	Mikac et al. (2023)[13]
PS	350 nm	Au@Ag colloid	Water	6.5 mg mL^{-1}	Ding et al. (2017)[36]
PS	1 μm and 100 nm	Au@Ag	Water, spinach, and kale	10 mg mL^{-1} or mg kg^{-1}	Kousheh et al. (2024)[3]
PE	1 μm and 65 nm	Au@Ag	Water, spinach, and kale	100 mg mL^{-1} or mg kg^{-1}	Hajikhani et al. (2024)[11]
PS	1 μm and 100 nm	BC@Au@Ag	Water, spinach, and kale	4 mg mL^{-1} or mg kg^{-1}	This study
PE	1 μm and 65 nm	BC@Au@Ag	Water, spinach, and kale	40 mg mL^{-1} or mg kg^{-1}	This study

kg^{-1} for PE and 10 mg kg^{-1} for PS.[3] Collectively, these studies highlight the persistent challenge of achieving balanced sensitivity across different polymer types. By contrast, the nanostructured BC-based SERS platform effectively narrows this detection gap, offering more balanced and reliable quantification across different polymer types. These advances can be ascribed to the unique physicochemical characteristics of the nanostructured BC matrix. The highly porous and intercon-
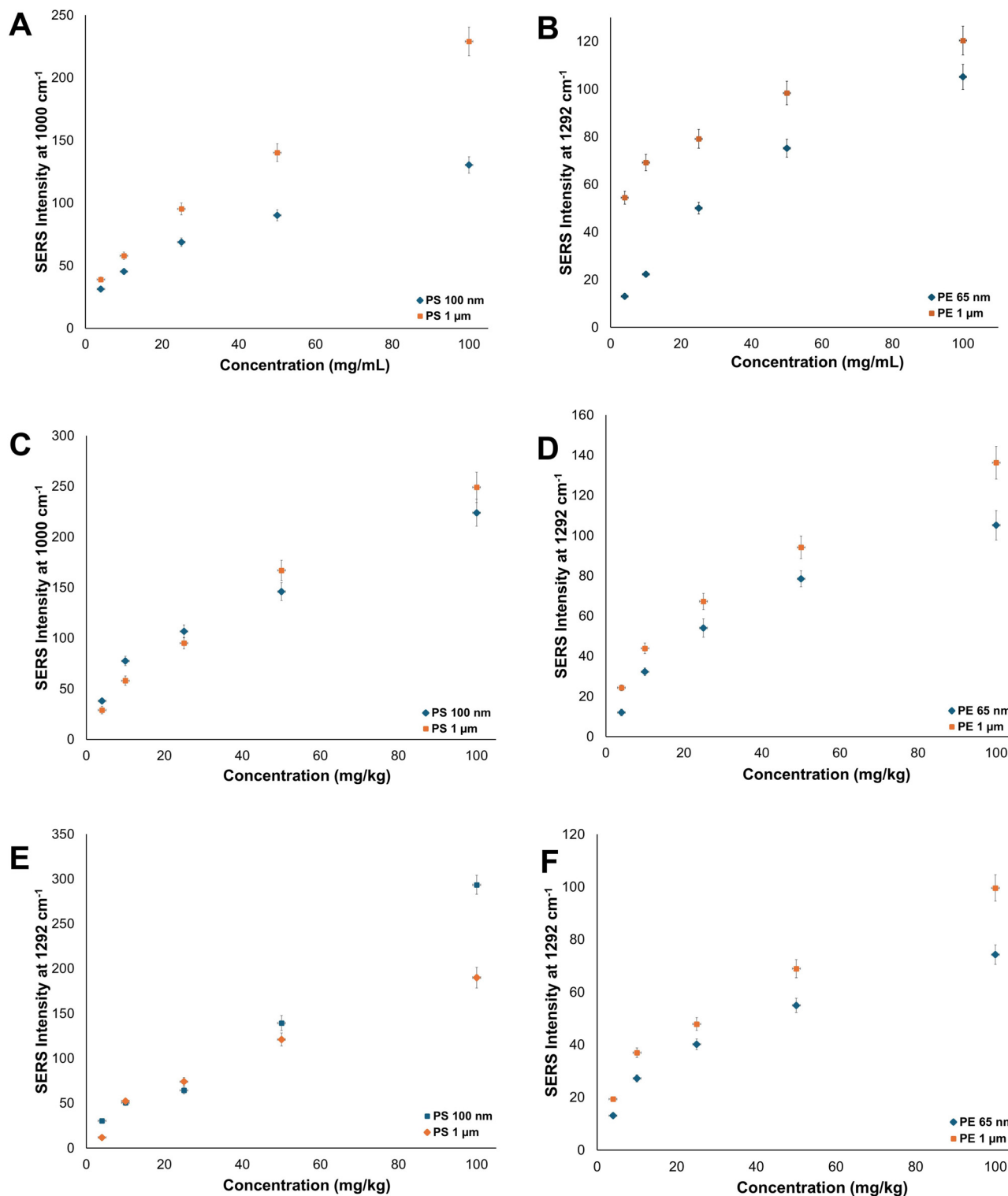

Fig. 6 Calibration plots constructed using the BC@Au@Ag sensor: polystyrene (1000 cm^{-1} peak) in water (A), spinach (C), and kale (E); polyethylene (1292 cm^{-1}) in water (B), spinach (D), and kale (F).

Table 3 The estimated limit of detection and limit of quantification of PS1, PS100, PE1, and PE65 in water, spinach, and kale (mg kg^{-1} or mg L^{-1})

	PS1	Spinach (PS1)	Kale (PS1)
LOD	3.38	9.77	12.55
LOQ	10.24	29.60	38.04
	PS100	Spinach (PS100)	Kale (PS100)
LOD	2.73	36.16	1.22
LOQ	8.26	109.58	3.70
	PE1	Spinach (PE1)	Kale (PE1)
LOD	4.97	48.74	45.77
LOQ	15.06	147.71	138.69
	PE65	Spinach (PE65)	Kale (PE65)
LOD	3.95	13.49	51.21
LOQ	11.96	40.88	155.20

Table 4 Quantitative spike-and-recovery performance and intra-/inter-day precision of PS and PE in kale using the BC@Au@Ag SERS platform ($n = 3$)

Analyte	Particle Size	Spike (mg kg^{-1})	% Recovery	Intra-day RSD%	Inter-day RSD%
PS	100 nm	4	167%	1.05	1.40
		10	140.3%	1.57	1.41
		25	76.3%	—	—
		50	93.0%	—	—
PS	1 μm	4	166.7	0.80	0.43
		10	159.8%	0.20	0.29
		25	114.3%	—	—
		50	111.8%	—	—
PE	65 nm	4	162.2	2.81	2.78
		10	127.0%	2.89	1.66
		25	139.5%	—	—
		50	120.1%	—	—
PE	1 μm	4	167.7%	1.04	0.35
		10	152.4%	0.55	0.22
		25	117.0%	—	—
		50	177.6%	—	—

nected fibrillar network of BC acts as an efficient scaffold that increases the probability of MNP entrapment, promotes uniform analyte adsorption, and maximizes analyte–substrate interactions. Furthermore, the intimate integration of BC with Au@Ag plasmonic nanostructures ensures the localization of target particles within electromagnetic "hot spots", thereby enhancing SERS efficiency. This synergistic architecture not only strengthens Raman signal intensity but also minimizes variability across particle size distributions, ultimately enabling sensitive and reproducible quantification of both nano- and microplastics in complex food matrices.

Matrix effects strongly influenced the sensitivity of detection and LOD/LOQ values among samples. Interestingly, vegetable samples exhibited lower LOD and LOQ values than water, despite their higher impurity content. This paradox may be explained by the presence of naturally occurring metal ions (*e.g.*, Fe, Zn, Mg), which can act as secondary Raman enhancers, and organic acids such as citrate in kale and spinach.[45,46] Citrate, in particular, is known to adsorb onto Au@Ag surfaces, modulate surface charge, and promote electrostatic attraction between nanoparticles and partially oxidized MNPs. These interactions enhance hot-spot formation and mitigate the hydrophobicity of PS and PE, thereby increasing SERS detectability.[47,48] While these interpretations are consistent with our results, future work should include controlled experiments (*e.g.*, ion or citrate spiking in water) to validate these matrix-dependent mechanisms and to disentangle beneficial effects from potential interferences by pigments, phenolics, or chlorophyll present in leafy vegetables.

Spike-and-recovery experiments in kale at concentrations of 10, 25, and 50 mg kg^{-1} further corroborate this matrix-dependent enhancement behaviour. Recoveries ranged from 76% to 178%, while maintaining low RSD values of 5–6%, underscoring the high analytical precision of the method even in a chemically complex matrix (Table 4). Recoveries above 100% indicate apparent recoveries relative to the selected calibration model and are likely due to matrix effects, specifically matrix-induced enhancement (*i.e.*, positive bias). Endogenous ions and organic acids in kale and spinach promote controlled nanoparticle aggregation, strengthen electromagnetic coup-

ling, and increase hot-spot density relative to aqueous standards. These matrix-mediated interactions elevate Raman intensities for equivalent analyte concentrations, yielding recoveries that reflect plasmonic amplification rather than quantitative bias. While this does not diminish the method's robustness, it highlights the necessity of matrix-matched calibration or standard addition approaches for accurate absolute quantification. Collectively, these recovery results confirm that the BC@Au@Ag platform performs reliably in real food matrices and reveal an opportunity to leverage intrinsic matrix chemistry for further optimization of SERS sensitivity.

In addition to recovery performance, the method's reproducibility, a longstanding challenge in SERS analysis, was evaluated at multiple levels. Spot-to-spot reproducibility was first assessed by collecting spectra from ten randomly selected locations on kale samples spiked with a high concentration of MNPs (1000 mg kg^{-1}). As shown in Fig. 7, the characteristic Raman peaks of PS and PE exhibited high spectral consistency, with RSD values below 10%, thereby confirming the spatial uniformity and stability of the BC@Au@Ag substrate.

To further assess method-level reproducibility beyond spatial variability, intra-day and inter-day precision were evaluated at lower concentrations (4 and 10 mg kg^{-1}), closer to the practical working range and the lowest detected concentration in this method. These assessments involved independent preparations of BC@Au@Ag substrates and full analytical workflows. Intra-day precision yielded exceptionally low RSD values ranging from 0.20% to 2.89%, while inter-day precision values ranged from 0.22% to 2.78% for both PS and PE across all evaluated particle sizes (Table 4). These values are substantially lower than those typically reported for SERS analyses in complex food matrices, demonstrating excellent day-to-day consistency.

Taken together, the combined recovery, spot-to-spot, intra-day, and inter-day precision results provide a comprehensive validation of the BC@Au@Ag SERS platform. Although matrix-
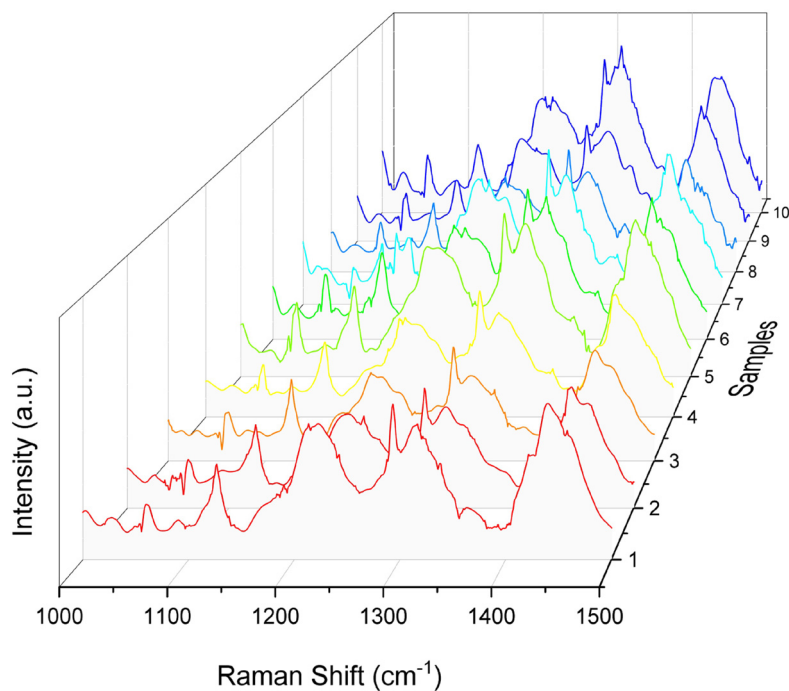
Fig. 7 SERS spectra acquired from ten random spots on a kale sample spiked with 1000 mg kg^{-1} of MNPs, showing the reproducibility of the BC@Au@Ag sensor (RSD = ±2.98%).

induced plasmonic amplification in kale contributes to elevated recoveries at higher concentrations, the consistently low RSD values across independent substrates and multiple days confirm the high reproducibility of the overall method, including substrate fabrication, sample preparation, and SERS measurement. This robustness strongly supports the applicability of the developed sensor for practical monitoring of MNP contamination in complex food matrices.

Conclusions

This research developed a novel SERS-based method to detect MNP contamination in food, addressing major limitations in sensitivity and reproducibility. By leveraging BC as both a structural matrix and an eco-friendly reducing agent, the study eliminates the need for toxic chemical reagents while enabling uniform deposition of Au@Ag core–shell nanoparticles. Among the evaluated synthesis strategies, Method M3 proved optimal, producing particles with well-controlled core–shell morphology. This configuration maximizes plasmonic resonance and generates high-density "hot spots" essential for signal amplification.

The BC@Au@Ag sensor demonstrated high analytical sensitivity, enabling detection of PE and PS MNPs in kale down to 4 mg kg^{-1}. Furthermore, theoretically estimated LODs, calculated from weighted regression analysis, reached as low as 1.22 mg kg^{-1} for PS and 3.95 mg kg^{-1} for PE, making substantial improvement over previously reported SERS-based methods. The sensor demonstrated robust performance across

aqueous and food matrices, delivering reproducible spectra of the samples. Matrix-specific enhancements, likely driven by components such as citric acid and trace metals in kale, further improved detection.

The BC nanofiber structure enhances the capture of nanoplastics through size-selective absorption, while the bimetallic Au@Ag composition improves signal intensity and stability. This synergistic architecture enables reliable detection of both micro- and nanoscale particles, thus, significantly reducing the sensitivity gap between them. The platform's green synthesis, cost-effective materials, and reproducibility make it a practical solution for integration into food safety and environmental monitoring workflows.

Future research should focus on expanding this technology to detect additional polymer types (*e.g.*, PVC, PET), integrating it with portable Raman systems for field diagnostics, and coupling it with machine learning for real-time spectral classification. This BC-based SERS platform marks a critical step toward scalable, routine, and environmentally responsible monitoring of plastic contamination in food and ecological systems.

Author contributions

S. K.: conceptualization, data curation, methodology, writing original draft and editing. A. M.: methodology, writing review and editing. M. L.: conceptualization, project administration, supervision, writing review and editing.

Conflicts of interest

The authors declare that they have no known competing financial interests or personal relationships that could have appeared to influence the work reported in this paper.

Data availability

All data underpinning this study are available in the article and its supplementary information (SI). Supplementary information is available. See DOI: https://doi.org/10.1039/d5an01043h.

Raw datasets generated and/or analyzed during the current study are available from the corresponding author upon reasonable request.

Acknowledgements

References

1 L. Yang, Y. Cai, H. Liu and R. Yang, *Anal. Chem.*, 2025, **97**, 5022–5028.
2 Statista, Plastics Industry in the U.S., https://www.statista.com/statistics/203398/total-us-resin-production/#:~:text=In%202023%2C%20the%20total%20plastics,purposes%2C%20and%20building%20and%20construction, (accessed 12 November 2025).
3 S. Kousheh, M. Hajikhani, S. Asgari and M. Lin, *Microchim. Acta*, 2024, **191**, 755.
4 J. G. R. de Carvalho, H. C. Augusto, R. Ferraz, C. Delerue-Matos and V. C. Fernandes, *Toxics*, 2024, **12**, 762.
5 A. Nene, S. Sadeghzade, S. Viaroli, W. Yang, U. P. Uchenna, A. Kandwal, X. Liu, P. Somani and M. Galluzzi, *Environ. Sci. Eur.*, 2025, **37**, 7.
6 F. Corami, B. Rosso, M. Roman, M. Picone, A. Gambaro and C. Barbante, *Mar. Pollut. Bull.*, 2020, **160**, 111606.
7 F. Huth, A. Govyadinov, S. Amarie, W. Nuansing, F. Keilmann and R. Hillenbrand, *Nano Lett.*, 2012, **12**, 3973–3978.
8 P. Li, Y. Lai, Q. Li, L. Dong, Z. Tan, S. Yu, Y. Chen, V. K. Sharma, J. Liu and G. Jiang, *Anal. Chem.*, 2022, **94**, 740–747.
9 M. Correia and K. Loeschner, *Anal. Bioanal. Chem.*, 2018, **410**, 5603–5615.
10 S. Kousheh and M. Lin, *Trends Food Sci. Technol.*, 2025, **159**, 10940.
11 M. Hajikhani, S. Kousheh, Y. Zhang and M. Lin, *Food Chem.*, 2024, **436**, 137703.
12 X. Weng and S. Neethirajan, *Trends Food Sci. Technol.*, 2017, **65**, 10–22.
13 L. Mikac, I. Rigó, L. Himics, A. Tolić, M. Ivanda and M. Veres, *Appl. Surf. Sci.*, 2023, **608**, 155239.
14 L. Xie, J. Lu, T. Liu, G. Chen, G. Liu, B. Ren and Z. Tian, *J. Phys. Chem. Lett.*, 2020, **11**, 1022–1029.
15 C. Liu, D. Xu, X. Dong and Q. Huang, *Trends Food Sci. Technol.*, 2022, **128**, 90–101.
16 S. A. Ogundare and W. E. van Zyl, *Cellulose*, 2019, **26**, 6489–6528.
17 Y. Liu, L. Lin, B. Yang, M. Huang, X. Huang, X. X. Chen, Z. Dai, S. Sun, Y. Yang and C. Li, *ACS Sustainable Chem. Eng.*, 2024, **12**, 1595–1604.
18 R. K. Gangwar, A. K. Pathak, F. Chiavaioli, M. H. Abu Bakar, Y. M. Kamil, M. A. Mahdi and V. K. Singh, *Coord. Chem. Rev.*, 2024, **510**, 215861.
19 C. Desmonda, S. Kar and Y. Tai, *Appl. Surf. Sci.*, 2016, **367**, 362–369.
20 S. A. Kousheh, M. Moradi, H. Tajik and R. Molaei, *Int. J. Biol. Macromol.*, 2020, **155**, 216–225.
21 A. C. Rodrigues, A. I. Fontão, A. Coelho, M. Leal, F. A. G. Soares da Silva, Y. Wan, F. Dourado and M. Gama, *New Biotechnol*, 2019, **49**, 19–27.
22 L. Lv, L. He, S. Jiang, J. Chen, C. Zhou, J. Qu, Y. Lu, P. Hong, S. Sun and C. Li, *Sci. Total Environ.*, 2020, **728**, 138449.
23 S. Asgari, L. Sun, J. Lin, Z. Weng, G. Wu, Y. Zhang and M. Lin, *Microchim. Acta*, 2020, **187**, 1.
24 O. Eskilson, S. B. Lindström, B. Sepulveda, M. M. Shahjamali, P. Güell-Grau, P. Sivlér, M. Skog, C. Aronsson, E. M. Björk, N. Nyberg, H. Khalaf, T. Bengtsson, J. James, M. B. Ericson, E. Martinsson, R. Selegård and D. Aili, *Adv. Funct. Mater.*, 2020, **30**, 2004766.
25 V. Hospodarova, E. Singovszka and N. Stevulova, *Am. J. Anal. Chem.*, 2018, **09**, 303–310.
26 B. V. Mohite and S. V. Patil, *Carbohydr. Polym.*, 2014, **106**, 132–141.
27 A. Ashori, S. Sheykhnazari, T. Tabarsa, A. Shakeri and M. Golalipour, *Carbohydr. Polym.*, 2012, **90**, 413–418.
28 H. Sun, H. Bi, X. Lin, L. Cai and M. Xu, *Polymers*, 2020, **12**, 164.
29 C. Babac, T. Kutsal and E. Pİşkİn, *Int. J. Nat. Eng. Sci.*, 2009, **3**, 1–2.
30 T. J. Jayeoye, C. Supachettapun and N. Muangsin, *Arabian J. Chem.*, 2023, **16**, 104552.
31 B. Zhang, C. Xie, J. Hu, H. Wang and Y. Gui, *Compos. Sci. Technol.*, 2006, **66**, 1558–1563.
32 X. Liu, *Organic Chemistry I*, Kwantlen Polytechnic University, 2021.
33 Y. Hosakun, K. Halász, M. Horváth, L. Csóka and V. Djoković, *Chem. Eng. J.*, 2017, **324**, 83–92.
34 V. Nava, M. L. Frezzotti and B. Leoni, *Appl. Spectrosc.*, 2021, **75**, 1341–1357.

35 F. Blancho, M. Davranche, H. El Hadri, B. Grassl and J. Gigault, *Environ. Sci. Technol.*, 2021, **55**, 8753–8759.

36 S. Y. Ding, E. M. You, Z. Q. Tian and M. Moskovits, *Chem. Soc. Rev.*, 2017, **46**, 4042–4076.

37 B. Sharma, R. R. Frontiera, A.-I. Henry, E. Ringe and R. P. Van Duyne, *Mater. Today*, 2012, **15**, 16–25.

38 Q. T. Lê, N. H. Ly, M. K. Kim, S. H. Lim, S. J. Son, K. D. Zoh and S. W. Joo, *J. Hazard. Mater.*, 2021, **402**, 123499.

39 E. Le Ru and P. Etchegoin, *Principles of Surface-Enhanced Raman Spectroscopy: and related plasmonic effects*, Elsevier, 2008.

40 W. Shao, S. Wang, H. Liu, J. Wu, R. Zhang, H. Min and M. Huang, *Carbohydr. Polym.*, 2016, **138**, 166–171.

41 D. T. B. De Salvi, H. Da, S. Barud, O. Treu-Filho, A. Pawlicka, R. I. Mattos, E. Raphael and S. J. L. Ribeiro, *J. Therm. Anal. Calorim.*, 2014, **118**, 205–215.

42 Z. Zhang, H. Shang, B. Xing and L. He, *Anal. Methods*, 2021, **13**, 2567–2574.

43 J. Caldwell, P. Taladriz-blanco, B. Rothen-rutishauser and A. Petri-fink, *Nanomaterials*, 2021, **11**, 1149.

44 S. R. Tadi, A. G. Shenoy, A. Bharadwaj, C. S. Sreelakshmi, C. Mukhopadhyay, K. Sadani and P. Nag, *F1000Research*, 2024, **13**, 670.

45 A. Razzak, T. Mahjabin, M. R. M. Khan, M. Hossain, U. Sadia and W. Zzaman, *Heliyon*, 2023, **9**, e21709.

46 B. Nemzer, F. Al-Taher and N. Abshiru, *Molecules*, 2021, **26**, 2515.

47 M. Wu, J. Lin, D. Zheng, Y. Yang, Z. Li, Z. Zhu, Y. Shen, G. Ni and M. Zhang, *Chemosensors*, 2023, **11**, 531.

48 P. Yu, C. Shen, X. Yin, J. Cheng, C. Liu and Z. Yu, *Foods*, 2025, **14**, 2109.